



## RESEARCH ARTICLE SUMMARY

## NEUROSCIENCE

## Brainstem control of vocalization and its coordination with respiration

Jaehong Park\*, Seonmi Choi, Jun Takatoh, Shengli Zhao, Andrew Harrahill, Bao-Xia Han, Fan Wang\*

**INTRODUCTION:** Phonation, the pivotal process governing vocalization and speech, requires two simultaneous actions of narrowing the larynx (vocal cord adduction) and exhaling air from the lungs. Speech cannot occur during inhalation, because inspiration dominantly inhibits vocalization. This breathing primacy is crucial for survival. Although prior studies have identified neurons in the midbrain periaqueductal gray (PAG) as a permissive gate for eliciting vocalizations, the alternating patterns of inspiration and vocalization are not changed by PAG stimulation in experimental animals. This prompted our investigation to identify a neural population directly driving phonation and to elucidate its interactions with the breathing circuit that ensure vocal-respiratory coordination and prioritize breathing. To this end, we used mouse ultrasonic vocalizations (USVs) as a model, in which vocal cord adduction is required for USVs and USV syllables are periodically interrupted by inspirations.

**RATIONALE:** Our hypothesis centers on laryngeal premotor neurons in the brainstem as being key controllers of vocal cord adduction and its coordination with breathing. Whereas

past literature has identified the nucleus of retroambiguus (RAM) in the caudal hind-brain as a critical node for vocalization, its heterogeneity, including neurons modulating respirations and other orofacial movements, necessitates precise targeting of vocalization-specific premotor neurons within the RAM to unravel the mechanistic intricacies of vocal cord control. Using monosynaptic rabies virus-mediated transsynaptic tracing, we labeled a population of excitatory laryngeal premotor neurons in the RAM in adult mice. Furthermore, courtship USVs induced robust expression of the immediate early gene *Fos* in these rabies-traced RAM neurons (RAM<sup>VOC</sup>), leading us to use a *Fos*-based targeting method (CANE) to label and manipulate RAM<sup>VOC</sup> neurons and examine their role in phonation and the vocal-respiration interaction.

**RESULTS:** Silencing RAM<sup>VOC</sup> neurons using tetanus toxin light chain abolished courtship USVs and pain-elicited audible squeaks in adult mice, along with a lack of phonation-related abdominal muscle activity, indicating that RAM<sup>VOC</sup> neurons are necessary for phonation. Optogenetic activation of RAM<sup>VOC</sup>

was sufficient to induce vocal cord closure to elicit USVs, with the duration of activation influencing USV syllable lengths and concurrent expiration periods. Inspiration needs could override RAM<sup>VOC</sup>-mediated vocal cord closure. Both laryngeal motoneurons and RAM<sup>VOC</sup> neurons receive inhibitory inputs from the preBötzing complex (preBötC), which is known for containing inspiration rhythm-generating neurons. Ablating inhibitory synapses in RAM<sup>VOC</sup> neurons compromised the inspiration gating of vocal cord adduction, resulting in abnormal hoarse vocalizations during inspiration periods upon PAG stimulation. Additionally, disinhibited RAM<sup>VOC</sup> led to spontaneous USVs in the absence of a social context.

**CONCLUSION:** Our study unveils the circuits and mechanisms underlying phonation and vocal-respiration interaction (see the figure). RAM<sup>VOC</sup> forms the critical premotor node downstream of PAG necessary for all phonations by driving vocal cord adduction and coordinating expiratory muscle activity. Furthermore, inhibitory inputs from the preBötC to both RAM<sup>VOC</sup> and laryngeal motoneurons enable rhythmic inspiration to gate and pace vocalization, thereby ensuring breathing primacy. ■

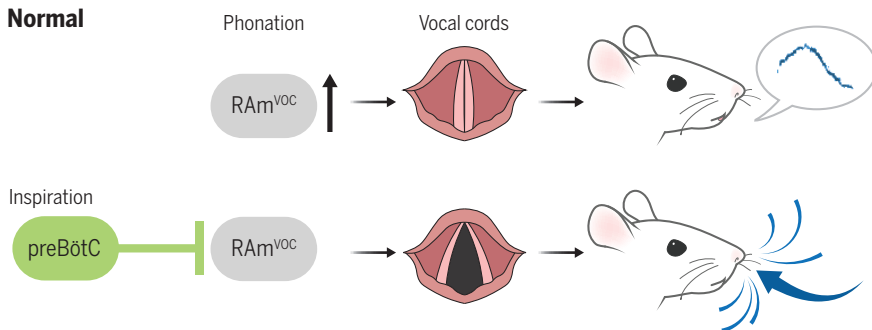
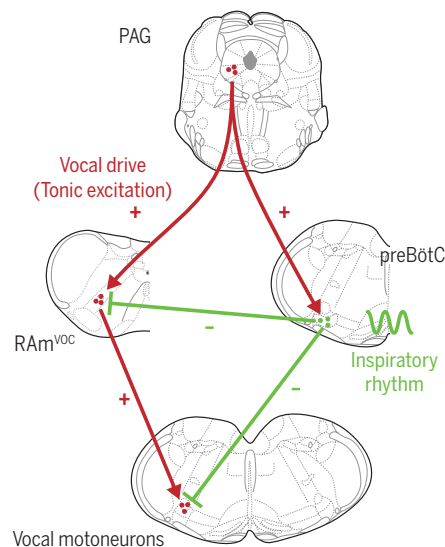
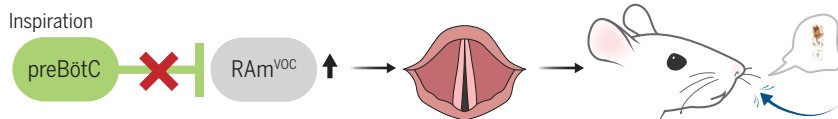
The list of author affiliations is available in the full article online.

\*Corresponding author. Email: fan\_wang@mit.edu (F.W.); jaehong@mit.edu (J.P.)

Cite this article as J. Park et al., *Science* 383, eadi8081 (2024). DOI: 10.1126/science.eadi8081

**S READ THE FULL ARTICLE AT**  
<https://doi.org/10.1126/science.eadi8081>

## Normal

Block synaptic inhibition to RAM<sup>VOC</sup>

**Neurons and circuit mechanisms for phonation and vocalization-respiration coordination.** RAM<sup>VOC</sup> represents vocal premotor neurons downstream of the PAG that drive vocal cord closure and phonations (ultrasonic vocalizations in mice). During inspiration, inhibitory neurons in the inspiration rhythm generator preBötC suppress activities of RAM<sup>VOC</sup> and vocal motoneurons to ensure breathing. Blocking inhibitory inputs to RAM<sup>VOC</sup> results in abnormal vocalization during inspiration.

## RESEARCH ARTICLE

## NEUROSCIENCE

## Brainstem control of vocalization and its coordination with respiration

Jaehong Park<sup>1,2\*</sup>, Seonmi Choi<sup>1</sup>, Jun Takahashi<sup>1</sup>, Shengli Zhao<sup>3</sup>, Andrew Harrahill<sup>1</sup>, Bao-Xia Han<sup>3</sup>, Fan Wang<sup>1\*</sup>

Phonation critically depends on precise controls of laryngeal muscles in coordination with ongoing respiration. However, the neural mechanisms governing these processes remain unclear. We identified excitatory vocalization-specific laryngeal premotor neurons located in the retroambiguus nucleus (RAM<sup>VOC</sup>) in adult mice as being both necessary and sufficient for driving vocal cord closure and eliciting mouse ultrasonic vocalizations (USVs). The duration of RAM<sup>VOC</sup> activation can determine the lengths of both USV syllables and concurrent expiration periods, with the impact of RAM<sup>VOC</sup> activation depending on respiration phases. RAM<sup>VOC</sup> neurons receive inhibition from the preBötzing complex, and inspiration needs override RAM<sup>VOC</sup>-mediated vocal cord closure. Ablating inhibitory synapses in RAM<sup>VOC</sup> neurons compromised this inspiration gating of laryngeal adduction, resulting in discoordination of vocalization with respiration. Our study reveals the circuits for vocal production and vocal-respiratory coordination.

Vocalization plays essential roles in communication in many species (1, 2). Although the complexity of vocalization (i.e., articulation) varies depending on species, the fundamental sound production process (i.e., phonation) shares similarities. The phonation process dominantly occurs during expiration: narrowing of the larynx (vocal cord adduction) while simultaneously exhaling air (3). In general, phonations do not happen during inhalation because inspiration requires opening of the larynx (vocal cord abduction) (4). Furthermore, the need for inspiration suppresses vocalization (breathing primacy)—everyday experience illustrates that we have to stop talking when we need to breathe. Inappropriate adduction or abduction of the larynx in the wrong respiration phases can lead to inspiration problems or hoarse vocalizations (5, 6). Lacking in our knowledge about vocalization is how neural circuits seamlessly coordinate laryngeal movements with respiration to produce phonations and to prioritize breathing needs.

We reasoned that the key to understanding this process is to first identify the neurons that drive laryngeal adduction for vocalization and then determine their interaction with respiratory circuits. The hindbrain contains premotor neurons that can activate laryngeal adductor motoneurons (1, 2, 7). The nucleus retroambi-

guus (RAM), which is located in the caudal-ventral brainstem, is one key node for vocal production. Vocalizations induced by electrical stimulation of the midbrain periaqueductal gray (PAG) in decerebrate cats (8, 9) and anesthetized rats (10) are suppressed by lesions of the RAM. Pharmacological and electrical stimulation of the RAM evokes elementary sounds (9–11), although such sounds do not resemble species-typical vocalizations. The RAM region has vocalization-related neural activity (12) and shows a positive correlation between unit activity and vocal loudness (13). Neural tracers injected in the RAM label axonal projections to the nucleus ambiguus (NA), where laryngeal motoneurons are located (14). However, the RAM region does not have anatomical demarcations and contains heterogeneous types of neurons, including those modulating respirations and other orofacial movements (15). Thus, it remains unknown which populations in the RAM are vocalization specific laryngeal premotor neurons, whether they are necessary and sufficient to drive vocal cord adduction and phonation, and, if so, how they interact with respiratory circuit to ensure vocal-respiration coordination and breathing primacy. With regard to respiration, intensive studies have been conducted on the inspiration rhythm generator, the preBötzing complex (preBötC) (16–19). However, only one study has investigated the function of the preBötC during vocalizations in awake animals (20). Therefore, it is still unclear how inspiration gates the activity of hindbrain vocal production circuits.

We used mouse ultrasonic vocalization (USV) as a model system. During interactions with female mice, male mice readily emit USVs

comprising a string of syllables periodically interrupted by inspiration, also called courtship songs (21, 22). Unlike audible vocalizations, which are produced by air vibrating the tightly closed vocal cords (23), USVs are produced by a whistle-like mechanism, a jet stream of air coming through a small hole formed between the adducted vocal cords (24–26), thereby generating pure-tone sounds in the ultrasonic frequency range. Despite this specific phonation mechanism, USVs still require laryngeal adduction and necessitate that this adduction occurs during expiration (24), thereby providing us with a suitable model for vocal-respiratory coordination.

## Vocalization-specific laryngeal premotor neurons in the brainstem

The activity of laryngeal muscles and motoneurons is controlled by premotor neurons in the hindbrain (1, 7). However, the location and identity of the vocal premotor circuits in adult mammals have yet to be revealed. We applied three-step monosynaptic rabies virus tracing (27) (Fig. 1A) combining retrograde adeno-associated virus (AAVretro)–Cre injected into laryngeal muscles in juvenile animals and Cre-dependent helper AAVs [to express TVA receptor and optimized rabies glycoprotein (oG) in motoneurons] and pseudotyped G-deleted rabies virus (EnvA<sup>M21</sup>-RV-GFP, where GFP is green fluorescent protein) both injected into the NA in adults. Cre<sup>+</sup> motoneurons were found around the NA (Fig. 1B), and trans-synaptically labeled laryngeal premotor neurons were mostly observed in the brainstem (Fig. 1C), specifically in the Kölliker-Fuse (KF), parvocellular reticular formation (PCrT), lateral paragigantocellular nucleus (LPGi), intermediate reticular nucleus (IRt), preBötC, nucleus tractus solitarii (NTS), and RAM. We registered all labeled neurons in the Allen Mouse Brain Common Coordinate Framework (hereafter, Allen CCF) (28) and compared the map of laryngeal premotor neurons with our previously identified maps of jaw and tongue premotor neurons (27) (fig. S1). The overall spatial distributions of laryngeal premotor neurons from different mice ( $n = 3$ ) were similar but distinct from those of jaw and tongue premotor maps (fig. S1). Labeled premotor neurons also had extensive collateral projections to other branchial motor nuclei, including the trigeminal (5N), the facial (7N), and the hypoglossal (12N) nuclei (fig. S1), suggesting that laryngeal premotor neurons might simultaneously recruit other orofacial motoneurons for vocalization and perhaps for other orofacial movements.

Previous studies have suggested that the RAM is a critical node for vocal production (7, 14). When we examined *Fos* mRNA expression (a marker for activated neurons) in male mice 90 min after female-induced

<sup>1</sup>Department of Brain and Cognitive Sciences, McGovern Institute for Brain Research, Massachusetts Institute of Technology, Cambridge, MA 02139, USA. <sup>2</sup>Department of Biomedical Engineering, Duke University, Durham, NC, 27708, USA. <sup>3</sup>Department of Neurobiology, Duke University Medical Center, Durham, NC, 27710, USA.

\*Corresponding author. Email: fan\_wang@mit.edu (F.W.); jaehong@mit.edu (J.P.)

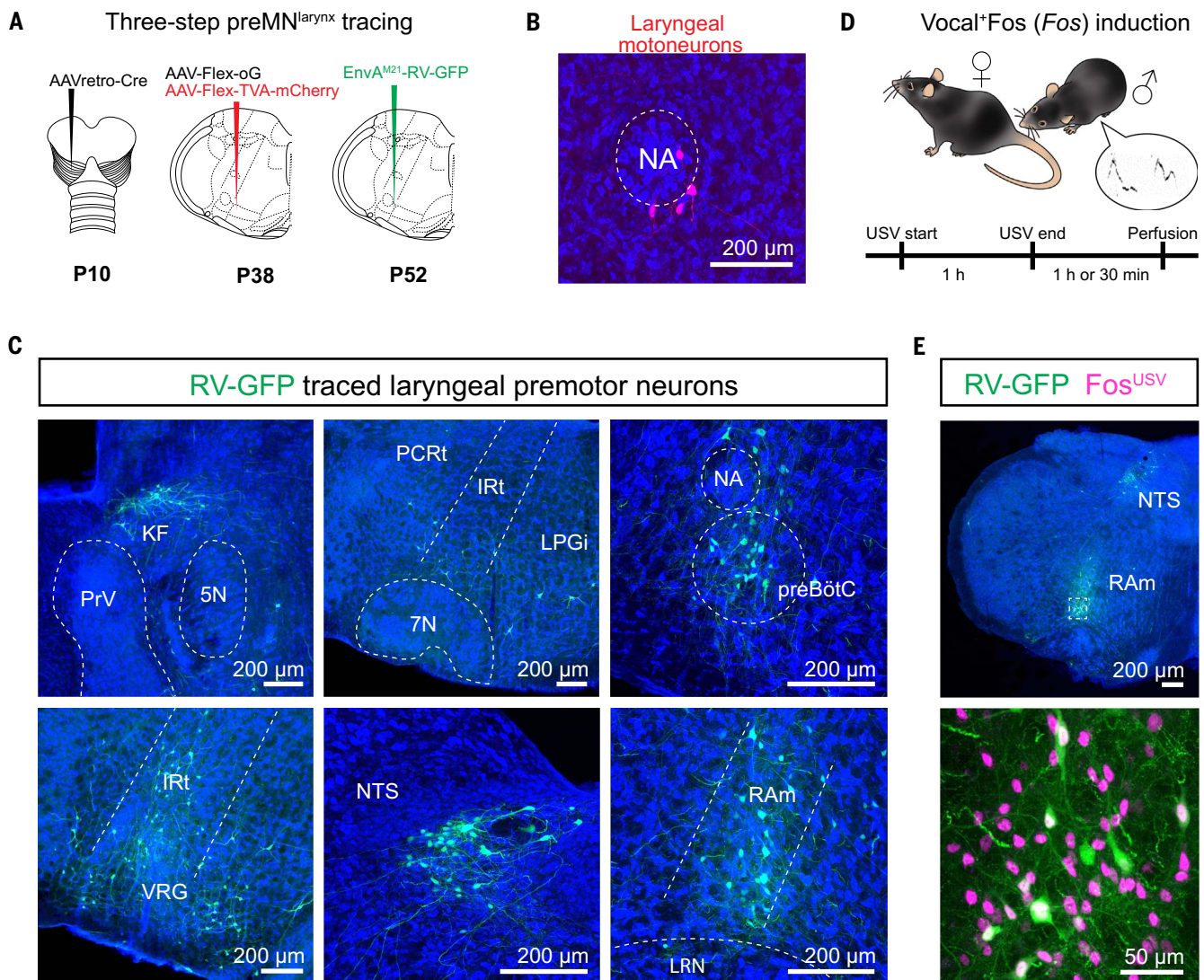


**Fig. 1. Transsynaptic mapping of laryngeal premotor neurons and vocalization-induced Fos activity in the RAM.** (A) Schematic of the three-step monosynaptic rabies virus strategy using AAVretro-Cre, helper virus (AAV-Flex-oG, AAV-Flex-TVA-mCherry) and monosynaptic rabies virus (EnvA<sup>M21</sup> coated) to map laryngeal premotor neurons. (B) Laryngeal motoneurons (red) labeled by AAVretro-Cre in the brainstem of an Ai-14 reporter mouse. (C) Laryngeal premotor neurons (green)

in the KF, PCrT, LPGi, preBötC, IRt, VRG, NTS, and RAM. (D) Schematic of Fos (1 h) or Fos mRNA (30 min) induction experiments in a social context eliciting USVs in male mice. (E) Laryngeal premotor neurons (green) and Fos (magenta) labeling in the RAM (top). A magnified image of the boxed area is shown at the bottom. Neurotrace Blue was used to visualize neuronal structures. Scale bars: 200  $\mu\text{m}$  in (B), (C), and (E), top; 50  $\mu\text{m}$  in (E), bottom.

courtship USVs (Fig. 1D), we detected robust Fos signals in the RAM (Fig. S2). By contrast, fewer and weaker sites of Fos expression were found in other hindbrain areas, such as the preBötC in the same samples (Fig. S2). Our laryngeal premotor tracing consistently labeled a cluster of RAM neurons (Fig. 1C). We further confirmed that the majority of rabies-traced laryngeal premotor neurons in the RAM induced Fos expression after bouts of courtship USVs ( $68.6 \pm 13.1\%$ , GFP<sup>+</sup> and Fos<sup>+</sup> neurons/GFP<sup>+</sup> neurons,  $n = 4$  mice, Fig. 1E).

We used the Fos-based cell targeting method called CANE (29) to label courtship USV-activated RAM neurons in male mice (RAM<sup>VOC</sup> neurons) (Fig. 2A). After expressing GFP in

RAM<sup>VOC</sup> neurons using CANE, we re-exposed male mice to females to re-elicited USVs and Fos expression and confirmed that labeled RAM<sup>VOC</sup> were indeed Fos<sup>+</sup> (Fig. 2B). We further registered the locations of all CANE-captured RAM<sup>VOC</sup> neurons in the Allen CCF and confirmed that their positions overlapped with those of the rabies-traced RAM laryngeal premotor neurons (Fig. 2C). We further examined the expression of choline acetyltransferase (ChAT), a molecular marker for motoneurons, and found that none of the labeled RAM<sup>VOC</sup> neurons expressed ChAT (Fig. 2D) (i.e., CANE did not capture cholinergic motoneurons). Furthermore, the axonal boutons from RAM<sup>VOC</sup>-GFP cells innervated ChAT<sup>+</sup> motoneurons around

the NA (Fig. 2D), consistent with their being vocal premotor neurons. Finally, in situ hybridization using *Vglut2* and *Vgat* probes showed that majority of RAM<sup>VOC</sup> neurons were glutamatergic (*Vglut2*<sup>+</sup>/RAM<sup>VOC</sup>:  $85.1 \pm 0.1\%$ , *Vgat*<sup>+</sup>/RAM<sup>VOC</sup>:  $12.9 \pm 0.1\%$ ,  $n = 3$  mice; Fig. 2E), suggesting that they provide excitatory inputs to laryngeal motoneurons.

#### Silencing RAM<sup>VOC</sup> neurons abolishes both ultrasonic and audible vocalizations

To determine the functional role of RAM<sup>VOC</sup> neurons, we bilaterally expressed tetanus toxin light chain (TeLC) to inhibit their synaptic outputs (30) or expressed GFP as controls using CANE (Fig. 2F). RAM<sup>VOC</sup>-GFP male mice

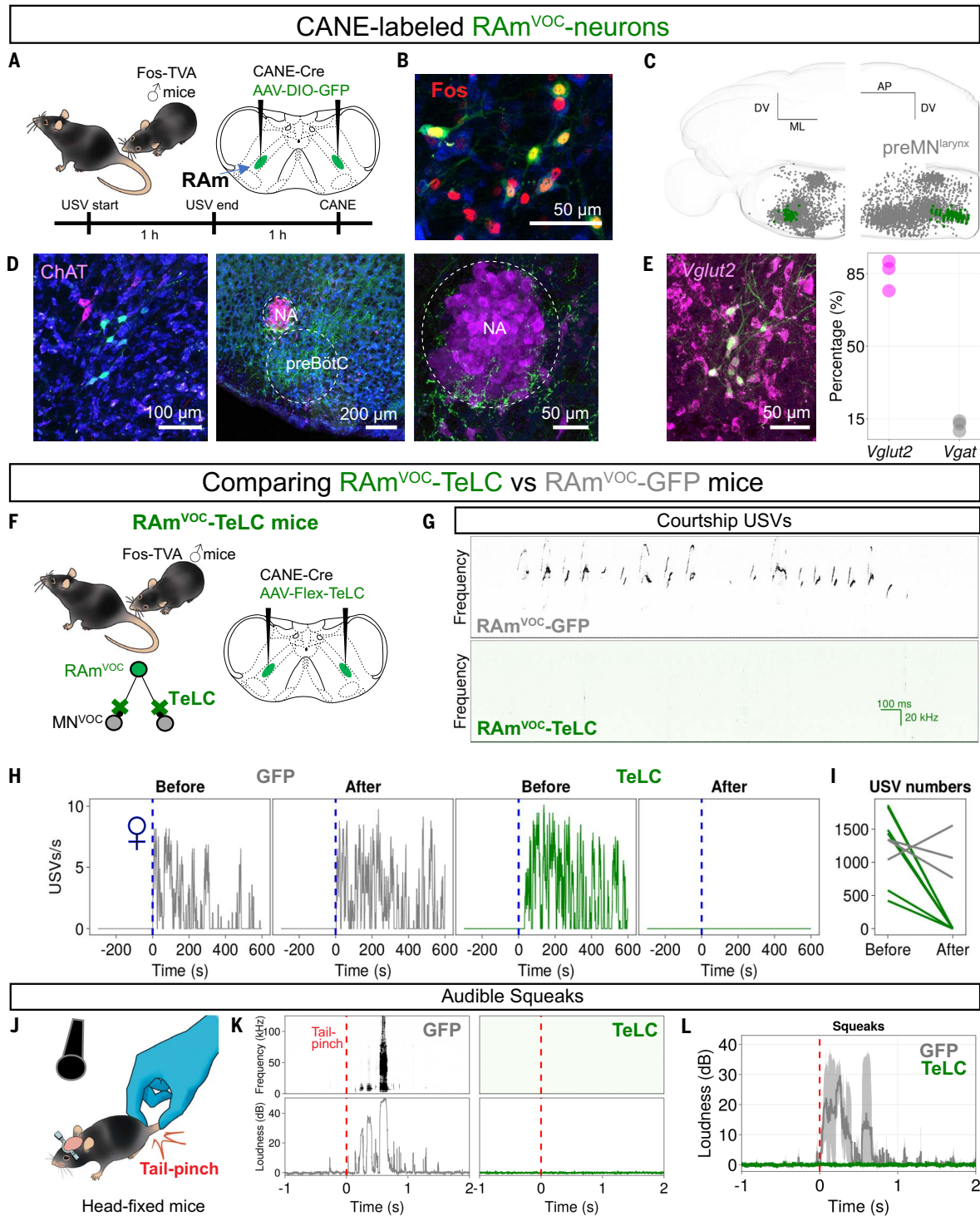


**Fig. 2.**  $\text{RAm}^{\text{VOC}}$  neurons are excitatory laryngeal premotor neurons and are required for vocalization in mice. **(A)** Schematic for CANE experiments to capture vocalization-induced  $\text{Fos}^+$  neurons in the RAM. **(B)**  $\text{RAm}^{\text{VOC}}$  neurons (green) with Fos immunolabeling (red). **(C)**  $\text{RAm}^{\text{VOC}}$  neurons (green) with the laryngeal premotor neurons (gray) in the Allen CCF in coronal (left) and sagittal (right) views. **(D)**  $\text{RAm}^{\text{VOC}}$  neurons (green) with ChAT immunolabeling (magenta). Left (soma) and middle (axon terminals). The right panel highlights the NA region of the middle panel. **(E)**  $\text{RAm}^{\text{VOC}}$  neurons (green) with fluorescent in situ hybridization labeling for *Vglut2* (magenta) (left). Group data of *Vglut2* and *Vgat* from  $n = 3$  mice. **(F)** Schematic for expressing TeLC in  $\text{RAm}^{\text{VOC}}$  neurons. **(G)** Spectrograms of female-directed USVs

of  $\text{RAm}^{\text{VOC}}$ -GFP control mice (top) and  $\text{RAm}^{\text{VOC}}$ -TeLC mice (bottom). **(H)** USV rates of male mice during courtship behaviors for 10 min. Blue vertical lines indicate the time of female introduction ( $\text{♀}$ ). Gray and green plots for a  $\text{RAm}^{\text{VOC}}$ -GFP mouse and a  $\text{RAm}^{\text{VOC}}$ -TeLC mouse before and 2 weeks after virus injection (left and right, respectively). **(I)** Total numbers of USV syllables during 10-min social interactions ( $\text{RAm}^{\text{VOC}}$ -TeLC, green,  $n = 6$ ; control, gray,  $n = 3$ ). **(J)** Schematic for recording tail pinch-induced audible squeaks. **(K)** Spectrogram (top) and sound intensity plots (bottom) of audible squeaks from  $\text{RAm}^{\text{VOC}}$ -GFP (gray, left) and  $\text{RAm}^{\text{VOC}}$ -TeLC (green, right) mice. Red vertical lines indicate the onset of tail-pinch stimuli. **(L)** Average intensity of squeaks during tail pinch ( $n = 3$  for each group).

emitted robust USVs in the presence of female mice before and after CANE-mediated expression (Fig. 2G, top, and H, left). By contrast,  $\text{RAM}^{\text{VOC}}$ -TeLC mice failed to vocalize in response to female mice after TeLC expression (Fig. 2G, bottom, and H, right). The effect of silencing  $\text{RAM}^{\text{VOC}}$  neurons was robust and consistent: All six  $\text{RAM}^{\text{VOC}}$ -TeLC mice had complete mutism during courtship (Fig. 2I).

In addition to social USVs, mice also elicit audible squeaks in response to strongly aversive stimuli (31). Prior studies suggested that USVs and squeaks are triggered by different neural pathways (31, 32). For example, a recent study showed that inhibition of the PAG-RAM pathway only abolished USVs, not pain-elicited audible vocalizations (32). We evoked squeaks in mice using a tail-pinch stimulus (Fig. 2J). Although control  $\text{RAM}^{\text{VOC}}$ -GFP mice responded with robust cries,  $\text{RAM}^{\text{VOC}}$ -TeLC mice were silent (Fig. 2, K and L). Furthermore, when we applied foot shocks,  $\text{RAM}^{\text{VOC}}$ -GFP (movie S1) mice, but not  $\text{RAM}^{\text{VOC}}$ -TeLC mice (movie S2), squeaked, even though all mice exhibited escape behaviors, indicating that nociceptive responses of the  $\text{RAM}^{\text{VOC}}$ -TeLC mice were intact.

To rule out the possibility that mutism in the  $\text{RAM}^{\text{VOC}}$ -TeLC mice originated from general breathing abnormalities, we habituated mice on a treadmill wheel and gently encouraged them to run (fig. S3). Running changes both the frequency and amplitude of breathing in mice (33). The modulation of respiration by running in  $\text{RAM}^{\text{VOC}}$ -TeLC mice remained intact, just as that in the control group. For  $\text{RAM}^{\text{VOC}}$ -TeLC ( $n = 3$ ) versus  $\text{RAM}^{\text{VOC}}$ -GFP ( $n = 4$ ), changes in inspiratory amplitude were as follows:  $27.8 \pm 8.4\%$  versus  $24.4 \pm 2.6\%$ ,  $P = 0.8597$ ; expiratory amplitude:  $12.6 \pm 6.6\%$  versus  $6.5 \pm 1.1\%$ ,  $P = 0.5959$ ; frequency:  $36.7 \pm 18.3\%$  versus  $27.3 \pm 9.5\%$ , respectively ( $P = 0.5959$ , Mann-Whitney  $U$  test; fig. S3).

We also observed some axon collaterals of  $\text{RAM}^{\text{VOC}}$  neurons in the thoracic spinal cord segment (fig. S4), where abdominal spinal motor neurons for active expiration are located, suggesting that  $\text{RAM}^{\text{VOC}}$  might be involved in increasing expiratory activity needed for generating sound (phonation). To test this idea, we measured abdominal electromyography (EMG) of anesthetized  $\text{RAM}^{\text{VOC}}$ -TeLC mice during PAG stimulation-induced vocalizations (fig. S4). A previous study has shown that optogenetic stimulation of RAM-projecting PAG neurons ( $\text{PAG}^{\text{RAM}}$ ) could reliably elicit USVs in mice (32).  $\text{PAG}^{\text{RAM}}$  neurons were labeled by injecting AAVretro-FlpO in the RAM, and injecting Flp-dependent optogenetic activator ChRmine (34) in the PAG, and in the same male mouse,  $\text{RAM}^{\text{VOC}}$  neurons were targeted to express either GFP or TeLC using CANE (fig. S4). Whereas  $\text{PAG}^{\text{RAM}}$  stimulation reliably elicited abdominal EMG activity concurrent with USVs in the GFP control mice,

the same stimulation failed to elicit USVs and abdominal EMG responses in the TeLC mice (fig. S4).

### $\text{RAM}^{\text{VOC}}$ activation is sufficient to elicit and modulate USVs in mice

In addition to active expiration, vocal production critically depends on vocal cord adduction. The nearly closed larynx is essential for the exhaling jet stream of air to whistle USVs or to vibrate the vocal cords to produce audible sounds (24–26). To determine whether  $\text{RAM}^{\text{VOC}}$  neurons are sufficient to close the vocal cords and elicit USVs, we expressed ChRmine in these neurons using CANE in male mice (Fig. 3A). First, the larynx was imaged with a camera while mice were anesthetized and placed in a prone position (Fig. 3B). The vocal cords naturally widened and narrowed (but not fully closed) rhythmically (Fig. 3C and movie S3), in phase with inhalation and exhalation, resulting in periodic changes in the size of the glottal area (Fig. 3D). Optogenetic activation of  $\text{RAM}^{\text{VOC}}$  with 5 s of continuous laser illumination instantaneously closed the vocal cords, and the laryngeal adduction persisted throughout the stimulation ( $n = 3$  mice; Fig. 3D and movie S3). This prolonged laryngeal adduction was interrupted by occasional glottal openings during the 5-s stimulation in all mice tested (this point is further elaborated below). We next stimulated  $\text{RAM}^{\text{VOC}}$  in awake male mice to determine whether this was sufficient to elicit USVs (Fig. 3E). Applying a brief 100-ms laser pulse reliably induced USVs time locked to each pulse (Fig. 3F). The onset latencies of the optogenetic-induced USVs were short ( $39.0 \pm 1.1$  ms; Fig. 3G). All  $\text{RAM}^{\text{VOC}}$  activation-elicited vocalizations were in the ultrasonic range ( $\text{RAM}^{\text{VOC}}$ -USV), and the syllable patterns of  $\text{RAM}^{\text{VOC}}$ -USVs included several typical types of female-directed USVs (35) (up, step-down, chevron, two-steps, short, but also unstructured ones; Fig. 3H). We also compared  $\text{RAM}^{\text{VOC}}$ -USVs and female-directed USVs for several acoustic features, and observed similar distributions for loudness, spectral purity, and pitch variance (Fig. 3I). The mean frequency of the  $\text{RAM}^{\text{VOC}}$ -USVs was different, i.e., lower than that of the female-directed USVs in the same mice ( $\text{RAM}^{\text{VOC}}$ -USVs:  $61.8 \pm 0.4$  kHz, female-directed:  $79.6 \pm 0.2$  kHz,  $P \leq 0.0001$ , Mann-Whitney  $U$  test), indicating that other neurons are needed for producing the full frequency range of natural USVs.

Given that a brief  $\text{RAM}^{\text{VOC}}$  activation elicited a single short USV syllable (Fig. 3F), we also tested whether  $\text{RAM}^{\text{VOC}}$  activation could alter the length of individual USV syllables. We varied the duration of optogenetic stimulation of  $\text{RAM}^{\text{VOC}}$  (50, 100, and 200 ms), and observed that indeed the lengths of  $\text{RAM}^{\text{VOC}}$ -USV syllables were proportionally correlated to the duration of laser stimuli (Fig. 4, B and D).

### Vocalization-respiration coordination during $\text{RAM}^{\text{VOC}}$ activation

For normal vocalization, sound is exclusively produced during the expiration phase (4). The results described above highlighted the role of  $\text{RAM}^{\text{VOC}}$  neurons in driving laryngeal adduction while coordinating expiration efforts. However, inspiration needs must be prioritized (breathing primacy) to ensure survival. To investigate the precise role of  $\text{RAM}^{\text{VOC}}$  in vocal-respiration coordination, we simultaneously measured USVs and respiratory activity in awake mice while optogenetically stimulating  $\text{RAM}^{\text{VOC}}$  with different durations (50, 100, and 200 ms) (Fig. 4, A to C). Longer  $\text{RAM}^{\text{VOC}}$  activation induced longer duration of expiration characterized by a flat period on the respiratory traces (Fig. 4, C and E). The durations of  $\text{RAM}^{\text{VOC}}$ -induced USVs and flat expirations were highly correlated ( $R^2 = 0.922$ ), consistent with the notion that  $\text{RAM}^{\text{VOC}}$  activity coordinately mediates vocal cord closure and expiration.

We next investigated whether the impact of  $\text{RAM}^{\text{VOC}}$  activation is dependent on the current ongoing respiratory phases. To test this idea, we analyzed the latencies and durations of  $\text{RAM}^{\text{VOC}}$ -induced flat expirations and USV syllables with respect to the onsets of laser  $\text{RAM}^{\text{VOC}}$  activation in respiration phases ( $F_{\text{laser}}$ ; Fig. 4F).  $\text{RAM}^{\text{VOC}}$  stimulation at the early expiration ( $F_{\text{laser}}$  during 0 to  $0.5\pi$ ) and late inspiration phases ( $F_{\text{laser}}$  during  $-0.5\pi$  to 0) produced longer durations of expirations and USVs with short latencies, whereas  $\text{RAM}^{\text{VOC}}$  activation in the late expiration ( $F_{\text{laser}}$  during  $0.5\pi$  to  $\pi$ ) and early inspiration phases ( $F_{\text{laser}}$  during  $-\pi$  to  $-0.5\pi$ ) elicited shorter expirations and shorter USVs with longer latencies (Fig. 4, G and H).

With 200 ms of  $\text{RAM}^{\text{VOC}}$  activation, we occasionally observed a full inspiration cycle during stimulation (200 ms; Fig. 4C). Similarly, in the anesthetized larynx-imaging preparation, the vocal cords were occasionally open during prolonged 5-s  $\text{RAM}^{\text{VOC}}$  activation, presumably due to an “override” by the need for inspiration (Fig. 3D). To further investigate this inspiratory gating of vocalization/vocal adduction in awake mice, we applied 2 s of continuous  $\text{RAM}^{\text{VOC}}$  activation. This 2-s stimulation produced multiple USV syllables accompanied by concurrent flat expiration periods, which were periodically interrupted by intervening inspirations (Fig. 4I). The amplitudes of the intervening inspirations were similar to those in the baseline conditions, indicating that these are normal breaths (Fig. 4I). We projected the onsets and offsets of the multiple USV syllables evoked by the 2-s  $\text{RAM}^{\text{VOC}}$  activation onto respiration phase maps (inspiration:  $-\pi$  to 0, expiration: 0 to  $\pi$ ; Fig. 4J). All syllables were exclusively found in the expiration phase (Fig. 4K), consistent with the notion that intervening inspirations can stop the ongoing USVs

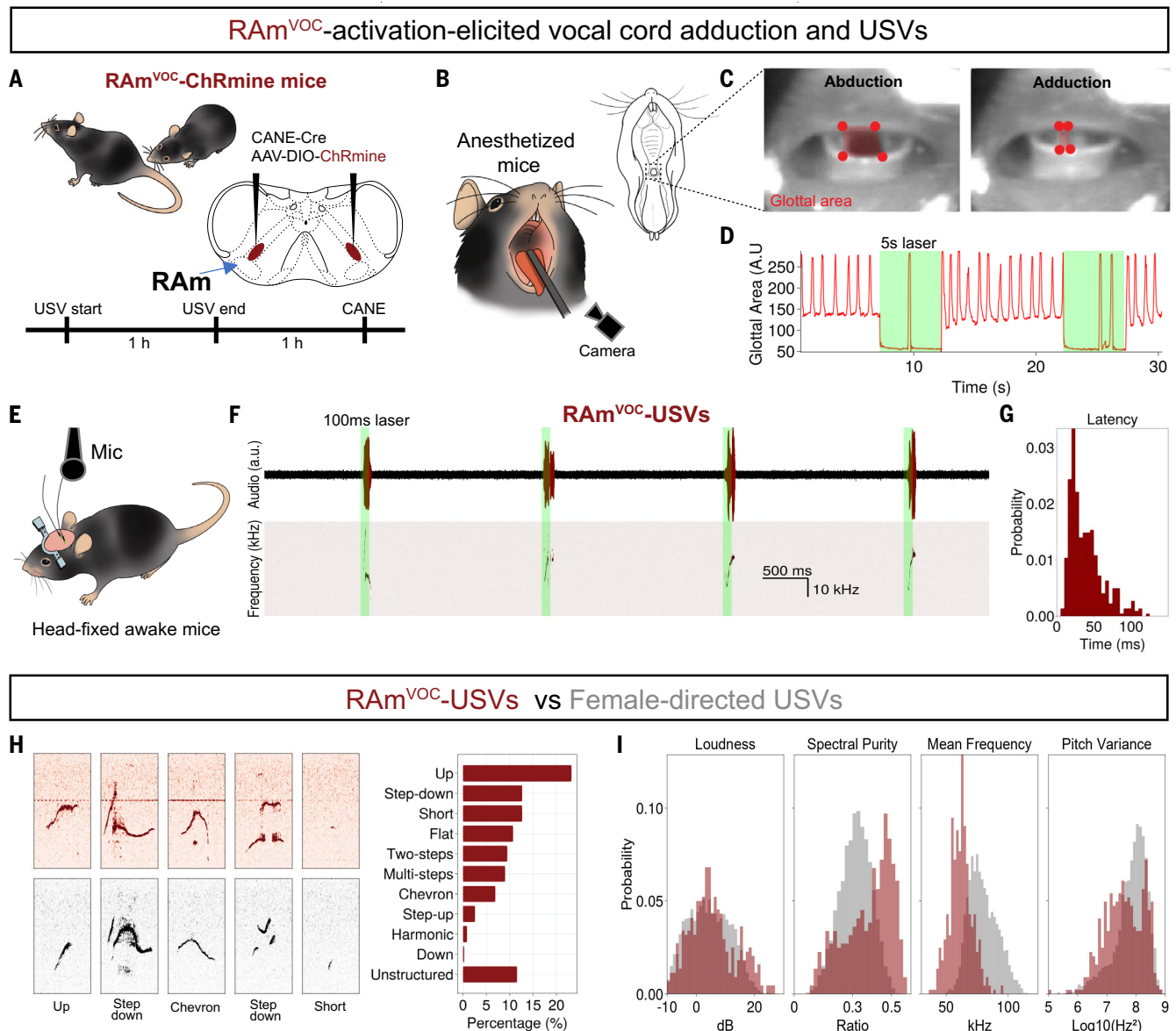


**Fig. 3. Optogenetic activation of RAM<sup>VOC</sup> neurons robustly elicits USV-like vocalizations in mice.** (A) Schematic for expressing ChRmine to RAM<sup>VOC</sup> neurons using the CANE method. (B) Schematic for visualizing the vocal cords in anesthetized mice. (C) Images showing opened (left) and closed (right) vocal cords. Red dots indicate the cartilage parts of the vocal cords that are used to track the glottal area (red rectangle). (D) Response of the glottal area to RAM<sup>VOC</sup> opto-activation. Green bar (5 s) indicates the laser stimulation period. (E) Schematic for recording vocalization of awake mice in a head-fixed condition. (F) Sound-time raw traces (top)

and corresponding frequency-time spectrogram (bottom) during a train of brief laser pulses (laser wavelength = 560 nm, 100 ms of 4 pulses with 2-s intervals). (G) Latency distribution of RAM<sup>VOC</sup>-USVs (laser duration: 100 ms, 443 syllables,  $n = 3$  mice). (H) Examples of RAM<sup>VOC</sup> (left top row, red) and female-directed USVs (left bottom row, gray). A single box spans 120 ms (x axis) and 30 to 125 kHz (y axis). Classification results of RAM<sup>VOC</sup>-USVs (right). (I) Distributions of four acoustic features (loudness, spectral purity, mean frequency, and pitch variance) of RAM<sup>VOC</sup>-USVs (443 syllables,  $n = 3$  mice) and female-directed USVs (4960 syllables,  $n = 3$  mice).

evoked by RAM<sup>VOC</sup> activation; i.e., inspiration gates and sets the basic rhythm of vocalization.

#### Inhibitory inputs to RAM<sup>VOC</sup> are essential for inspiration gating of vocalizations

We hypothesized that inhibitory inputs onto RAM<sup>VOC</sup> neurons are the key for the periodic suppression of vocalization by inspiration. To identify the source of inspiration-related inhibitory inputs to the RAM<sup>VOC</sup> neurons, we performed monosynaptic tracing of presynap-

tic neurons to RAM<sup>VOC</sup> (preRAM<sup>VOC</sup>). This was achieved by expressing TVA and oG in RAM<sup>VOC</sup> using CANE, followed by infecting these neurons with EnvA<sup>M21</sup>-RV-GFP (Fig. 5A). Tracing results showed that RAM<sup>VOC</sup> neurons receive excitatory inputs from the PAG, the parabrachial (PB), KF, and other areas (Fig. 5B). Excitatory PAG neurons are known to be required for eliciting USVs but not for generating rhythmic vocal patterns (32). The dominant source of inhibitory inputs to RAM<sup>VOC</sup> neu-

rons was the preBötC (Fig. 5B), the inspiration rhythm generator (19). In our mapping of laryngeal premotor neurons, we also labeled a population of inhibitory neurons in the preBötC (fig. S5). Thus, the preBötC provides inhibitory inputs to both vocal motoneurons (MN<sup>VOC</sup>) and to RAM<sup>VOC</sup> (Fig. 5C), consistent with a recent axonal tracing study of inhibitory preBötC neurons (36). These results suggest that the inspiration-controlled periodic patterns of USVs could be generated by tonic

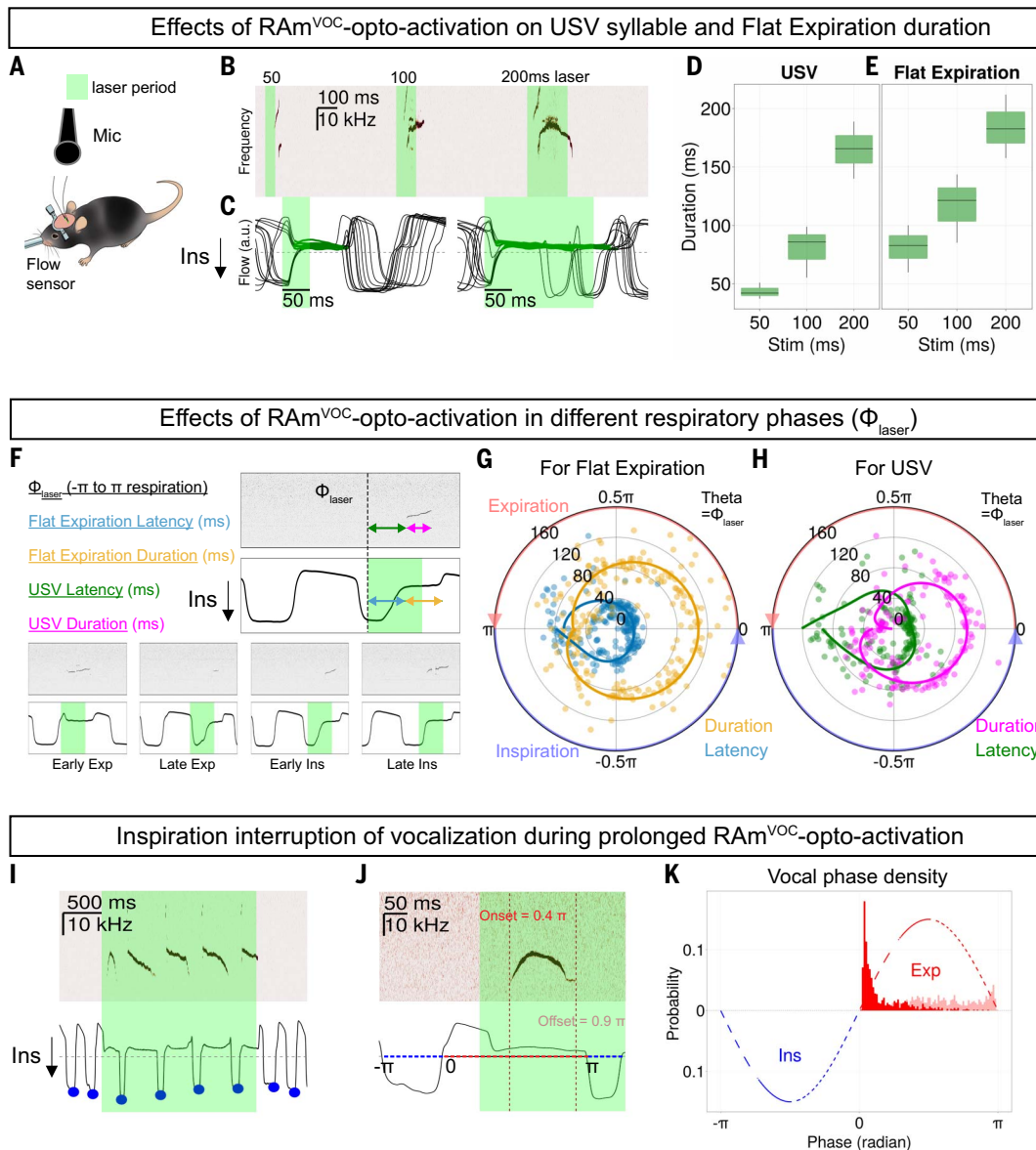


**Fig. 4. RAM<sup>VOC</sup> activation can modulate the duration of USVs and concurrent expiratory periods until interrupted by the need for breathing.** (A) Schematic for recording vocalization and respiration in RAM<sup>VOC</sup>-ChRmine mice. (B) USV syllables evoked by three different durations of RAM<sup>VOC</sup> laser activation (50, 100, and 200 ms). (C) Respiratory responses to the RAM<sup>VOC</sup> activation (left: 50 ms; right: 200 ms). Thirteen trials are aligned to the laser onsets and overlaid. Green lines indicate RAM<sup>VOC</sup>-induced flat expiration periods. (D) Average duration of RAM<sup>VOC</sup>-USVs ( $n = 3$  mice). (E) Average duration of RAM<sup>VOC</sup>-induced flat expiration periods ( $n = 3$  mice). (F) Schematic for defining laser stimulation phase ( $\Phi_{\text{laser}}$ ) and latency and duration of RAM<sup>VOC</sup>-induced flat expiration and USV to stimulation (top). Black trace indicates normalized airflow.  $\Phi_{\text{laser}}$  is defined as a phase of

laser onsets with respect to the expected airflow (inspiration:  $-\pi$  to 0; expiration: 0 to  $\pi$ ). Four cases of different stimulation onset phases (bottom). (G) Relationship between  $\Phi_{\text{laser}}$  and latency and duration of RAM<sup>VOC</sup> expirations (rho, ms scale). The same-color solid lines represent polynomial-fitted lines. Red and blue circle arrows indicate the expiration (0 to  $\pi$ ) and inspiration phases ( $-\pi$  to 0), respectively. (H) Relationship between  $\Phi_{\text{laser}}$  and latency and duration of RAM<sup>VOC</sup>-USVs. (I) USVs (top) and respiratory responses (bottom) to the 2-s RAM<sup>VOC</sup> activation. Blue dots indicate the inspiratory flow peaks. (J) Projection of onset and offset of a RAM<sup>VOC</sup>-USV onto a respiratory phase. (K) Phase density distribution of the onsets (red) and offsets (pink) of RAM<sup>VOC</sup>-USVs. Blue and red dashed lines represent arbitrary inspiration and expiration phases, respectively.

excitatory inputs from the PAG to RAM<sup>VOC</sup> to induce vocal cord adduction (and concurrent expiration), which is gated by rhythmic inhibition from the preBötC to both MN<sup>VOC</sup> and RAM<sup>VOC</sup> (Fig. 5C).

To validate the functional relevance of the anatomical connections identified above, we

decided to block inhibitory inputs to RAM<sup>VOC</sup> neurons. On the basis of the circuit diagram, we predicted that disinhibited RAM<sup>VOC</sup> would provide stronger and tonic excitatory drive to MN<sup>VOC</sup>, which counters the rhythmic inhibitory drive from the preBötC, such that vocal cord adduction may happen even during in-

spiration. Furthermore, if the activity of disinhibited RAM<sup>VOC</sup> was sufficiently elevated, spontaneous vocalization (in the absence of social interactions) might occur. We expressed GFE3 in glutamatergic RAM<sup>VOC</sup> neurons using CANE (RAM<sup>VOC</sup>-GFE3 mice), with RAM<sup>VOC</sup>-GFP mice as a control (Fig. 5D). This was achieved

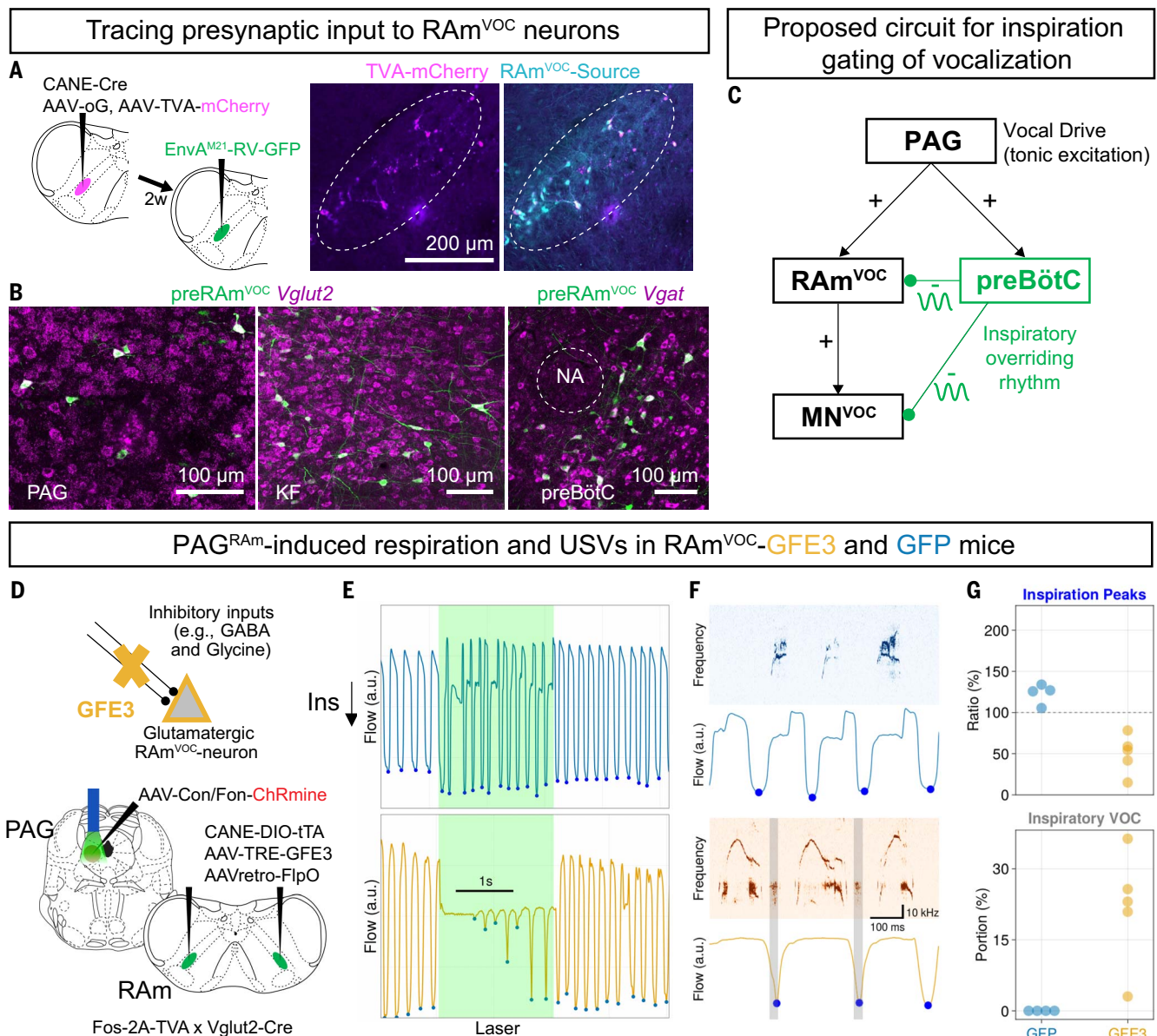


**Fig. 5. Ablating inhibitory synapses on  $RAM^{VOC}$  neurons compromised vocal-respiratory coordination.** (A) Schematic for transsynaptically tracing pre $RAM^{VOC}$  neurons (left). CANE and rabies labeled source cells (magenta, TVA; cyan, GFP) in RAM (right). Dashed circles indicate RAM areas. (B) pre $RAM^{VOC}$  neurons (green) in the PAG, KF, and preBötC with in situ hybridization (magenta) for *Vglut2* and *Vgat*. (C) Schematic for the proposed neural mechanism for vocal-respiratory coordination. (D) Schematic for ablating inhibitory synapses in  $RAM^{VOC}$  neurons with GFE3 expression ( $RAM^{VOC}$ -GFE3), and concurrent expression of ChRmine in RAM-projecting glutamatergic PAG neurons.

(E) Respiratory activities of the  $RAM^{VOC}$ -GFP (blue) and  $RAM^{VOC}$ -GFE3 (orange) mice in response to the  $PAG^{RAM/vglut2}$ -ChRmine stimulation for 2s. Blue dots represent the inspiratory peaks. (F) Spectrogram (top) with the respiratory responses (bottom). Gray bars label abnormal vocalizations in the inspiratory phases. (G) Average changes in the inspiratory peaks of the mice ( $n = 5$  GFE3 and  $n = 4$  GFP, top) during the  $PAG^{RAM/vglut2}$  stimulation over the baseline inspirations. The portions of the abnormal inspiratory vocalization among the  $PAG^{RAM/vglut2}$ -induced vocalizations ( $n = 5$  GFE3 and  $n = 4$  GFP, bottom). No inspiratory vocalization was detected in the GFP control mice.

by injecting Cre-dependent CANE-hSyn-DIO-tTA together with AAV-TRE3G-GFE3 (or GFP) in the RAM in *Fos<sup>TVA</sup>/Vglut2-Cre* double-transgenic male mice after bouts of courtship USVs. GFE3 is a ubiquitin ligase specifically targeting the inhibitory postsynaptic scaffolding protein gephyrin for degradation (37), thereby reducing phasic synaptic inhibition onto  $RAM^{VOC}$  neurons. To reliably elicit USVs

in awake head-fixed mice, we again chose to perform optogenetic stimulation of RAM-projecting PAG neurons ( $PAG^{RAM}$ ) (32). Briefly, in the same  $RAM^{VOC}$ -GFE3 or control mice, we also expressed ChRmine in RAM-projecting *Vglut2<sup>+</sup>* PAG neurons ( $PAG^{RAM/vglut2}$ ) using a Fip/Cre intersectional strategy (Fig. 5D). In control  $RAM^{VOC}$ -GFP mice, continuous pulses of optogenetic stimulation of  $PAG^{RAM/vglut2}$  re-

liably elicited USVs, but only during expirations, as the expirations were periodically interrupted by the inspiration flows (Fig. 5, E and F, top panels). In addition, the peak flow values for the inspiration (downward trace) increased during the optogenetic PAG stimulation ( $123.1 \pm 6.1\%$ ,  $n = 4$  mice; Fig. 5, E and G), suggesting that  $PAG^{RAM/vglut2}$  activation enhances inspiration (likely for inhaling sufficient air for

vocalization). By contrast, in  $\text{RAM}^{\text{VOC}}\text{-GFE3}$  mice, the inspiratory interruption of vocalization was severely compromised during continuous  $\text{PAG}^{\text{RAM/vglut2}}$  activation (Fig. 5E, bottom panels). The amplitude of the few intervening inspirations during PAG stimulations was significantly reduced compared with the average inspiration peak before stimulation ( $49.6 \pm 10.5\%$ ,  $n = 5$  mice,  $P = 0.020$ , Mann-Whitney  $U$  test for GFE3 versus GFP mice; Fig. 5, F and G, bottom panels). We observed that asthma-like vocal sounds were produced during the inspiration periods in  $\text{RAM}^{\text{VOC}}\text{-GFE3}$  (21.8  $\pm$  5.4%,  $n = 5$  mice; Fig. 5, F, gray-shaded region, and G), whereas these abnormal inspiratory vocal sounds were never observed in the  $\text{RAM}^{\text{VOC}}\text{-GFP}$  control mice during  $\text{PAG}^{\text{RAM/vglut2}}$  activation. Thus, removing inhibitory synaptic inputs to  $\text{RAM}^{\text{VOC}}$  neurons compromises inspiration gating of vocalization. The reduced inspiration amplitude is likely caused by persistent vocal cord adduction due to a tonic excitatory drive from the disinhibited  $\text{RAM}^{\text{VOC}}$ . This persistent vocal cord adduction during inspiration could also explain the abnormal asthma-like inspiratory vocalizations. Finally, consistent with the idea that tonic activation of disinhibited  $\text{RAM}^{\text{VOC}}$  neurons would cause spontaneous vocal cord closures,  $\text{RAM}^{\text{VOC}}\text{-GFE3}$  mice also produced occasional spontaneous USVs in the absence of social contexts ( $0.5 \pm 0.2$  VOC/s,  $n = 6$  mice; fig. S6), whereas control male mice almost never utter spontaneous USVs.

## Discussion

We found that a vocalization-specific laryngeal premotor population in the RAM region of the caudal hindbrain ( $\text{RAM}^{\text{VOC}}$ ) is the critical node for driving laryngeal adduction and phonation. We further uncovered neural mechanisms involving preBötC- $\text{RAM}^{\text{VOC}}$  interactions that ensure breathing primacy by allowing rhythmic inspirations to pace vocalizations. It has been debated whether the neural circuits for laryngeal adduction and vocal production are distributed across the ventral brainstem (7) or localized in one small area such as the RAM (14). Here, we found that inhibition of  $\text{RAM}^{\text{VOC}}$  neurons not only abolished USVs in social contexts but also audible squeaks during aversive states (tail pinch or foot shock). Thus,  $\text{RAM}^{\text{VOC}}$  represents a singular necessary locus for all phonations. Conversely, optogenetic stimulation of  $\text{RAM}^{\text{VOC}}$  neurons was sufficient to produce and only produced USVs, not audible sounds. USVs and squeaks in rodents have different acoustic features. USVs lie above ultrasonic range ( $>20$  kHz) and have pure tones (21, 22), and rodents use aerodynamic mechanisms to produce USVs (24–26), whereas audible squeaks occupy a human hearing frequency range ( $<20$  kHz) and have harmonics (38). Thus, squeaks likely require additional circuit elements, such as those

driving strong air exhalation, which are not activated or recruited by  $\text{RAM}^{\text{VOC}}$ .

USVs can be further modulated in terms of frequency and duration. The duration of mouse vocalizations could be modulated by  $\text{RAM}^{\text{VOC}}$  activity, but the mean frequency of  $\text{RAM}^{\text{VOC}}$ -USVs were lower than those of female-directed USVs in the same animals (Fig. 3). These data suggest that another parallel premotor pathway to laryngeal motor neurons (e.g., to vocal tensor muscles, such as cricothyroid muscles) might be involved in vocal frequency regulation. One potential frequency modulating region is the PCRt, which contains laryngeal premotor neurons, as shown in our trans-synaptic tracing study (Fig. 1C). This region, referred to as the vocalization-related parvocellular reticular formation in rats, is a node for high-frequency vocalization (10). For duration modulation, we showed that optogenetically increasing the time of  $\text{RAM}^{\text{VOC}}$  activation elongated the syllable length (Fig. 4, B and D). Trans-synaptic tracing of pre- $\text{RAM}^{\text{VOC}}$  neurons labeled inputs in the PB and KF (Fig. 5B), which could be the endogenous region controlling  $\text{RAM}^{\text{VOC}}$  activation and vocal duration based on previous pharmacological studies (39). However, the PB and KF regions are heterogeneous and include intermingled non-vocal respiratory neurons (40, 41), so future work targeting vocal-specific PB and KF will be needed to reveal their precise role in controlling vocal durations. Furthermore, it will be interesting to know whether and how the other recently identified brainstem vocal modulatory loci, the iRO, in neonate mice (42) interacts with  $\text{RAM}^{\text{VOC}}$  to modulate other features of vocalizations.

Breathing is vital for survival. Because breathing and vocalization both occur in the airway, laryngeal closure for sound production needs to be precisely controlled and coordinated with respiration. Failure in such coordination could lead to vocal cord dysfunction and breathing problems (5, 6). We found evidence of inspiration dominance over  $\text{RAM}^{\text{VOC}}$ -USVs: The effect of brief  $\text{RAM}^{\text{VOC}}$  activation was delayed and attenuated around the onset of inspirations; USV syllables produced by prolonged- $\text{RAM}^{\text{VOC}}$  activation were periodically interrupted by full inspiration peaks (Fig. 4). We found that the inspiration rhythm generator preBötC, where  $Vgat^+$  and  $GlyT2^+$  neurons are found (36, 43), provides the main source of inhibitory inputs to  $\text{RAM}^{\text{VOC}}$  (Fig. 5). Chronic disinhibition of  $\text{RAM}^{\text{VOC}}$  in  $\text{RAM}^{\text{VOC}}\text{-GFE3}$  experiments reduced the amplitudes of inspiratory gating during vocalization and produced hoarse sounds in inspiration phases, as well as spontaneous USVs in the absence of social context (Fig. 5 and fig. S6). Taken together, our results support a conceptual model (Fig. 5C) in which the timing of phonation is controlled by the combined activity of preBötC

and  $\text{RAM}^{\text{VOC}}$ , with inspiration playing a dominant role in setting the basic rhythm of vocalization and  $\text{RAM}^{\text{VOC}}$  driving vocal cord closure and modulating syllable durations within the limit set by inspiration. This mechanism produces the periodic alternating patterns of vocalization and inspiration. In human speech, multiple syllables can be uttered within one breath, so a separate multisyllable rhythm generator within the expiration period might be needed. We also labeled laryngeal premotor neurons in the NTS (Fig. 1C), which is a region receiving inputs from vagal pulmonary afferents (43). It is possible that the pulmonary-NTS pathway is involved in the transition between inspiration and vocalization (44). When the lungs are inflated with enough air, this pathway may help to inhibit the activity of preBötC and facilitate the transition to vocalization and expiration. Future work should test whether the pulmonary-NTS circuit represents the third node in modulating vocal patterns.

Finally, we want to point out that our study focused only on the “phonation,” not the complex “articulation” aspect of vocalization. Vocal articulations are among the most complicated motor patterns generated by humans (and many mammals) because they require coordinated control of the laryngeal, facial, tongue, jaw, and respiratory muscles. How this is achieved remains poorly understood. In our trans-synaptic tracing studies, we labeled a large population of neurons in the reticular formation and found that laryngeal premotor neurons also project to other orofacial motor nuclei (fig. S1). However, the identities of these premotor neurons are unknown, and more work will be needed to determine whether and how they are involved in complex articulations.

## Materials and methods

### Experimental models and subject details

All animal experiments were performed in accordance with the MIT Committee for Animal Care Use and Duke University Institutional Animal Care. Pups (approximately postnatal days 10 to 17) of either C57BL/6 or tdTomato reporter mice (Ai14, The Jackson Laboratory #007914) were used for tracing premotor neurons of the laryngeal muscles. Male homozygous  $\text{Fos}^{\text{TVA}}$  (The Jackson Laboratory #027831) were used for most of CANE experiments except for pre- $\text{RAM}^{\text{VOC}}$  tracing. Male heterozygous  $\text{Fos}^{\text{TVA}}$  (crossed with a C57BL/6 background) were used for pre- $\text{RAM}^{\text{VOC}}$  tracing.  $\text{Vglut2-ires-Cre}$  mice (The Jackson Laboratory #016963) were crossed with  $\text{Fos}^{\text{TVA}}$  mice to obtain  $\text{Fos}^{\text{TVA}}$  (het)/ $\text{Vglut2-ires-Cre}$  (het) for a subset of experiments.

### Viruses

The viruses used were as follows: AAV2retro-pENN.AAV.hSyn.Cre.WPRE.hGH (Addgene

#105553); AAV2retro-phSyn1(S)-FlpO-bGHpA (Addgene #51669); AAV2/8-CAG-Flex-oG (Addgene #48332, Duke Viral Vector Core); AAV2/8-CAG-Flex-TVA-mCherry (Addgene #74292, Duke Viral Vector Core); AAV2/8-hSyn-Flex-TeLC-P2A-EYFP-WPRE (Addgene #135391); AAV2/8-hSyn-DIO-EGFP (Addgene #50457); AAV2/8-nEF-Con/Foff 2.0-ChRmine-oScarlet (Addgene #137161); AAV2/8-nEF-Con/Fon-ChRmine-oScarlet (Addgene #137159); AAV2/8-nEF-Coff/Fon-ChRmine-oScarlet (Addgene #137160); AAV2/8-TRE3G-GFP-GFE3 (this study); AAV2/8-TRE3G-EGFP (this study); EnvA (M21)-RV-ΔG-GFP (29); CANE (lenti)-hSyn-Cre (29); and CANE (lenti)-hSyn-DIO-tTA (this study).

### Stereotaxic virus injection surgery

Mice were initially anesthetized by isoflurane (3%), then further maintained by isoflurane (1 to 2%) until the surgeries ended. The heads of mice were fixed at a stereotaxic frame (model 963, David Kopf Instruments), and the body temperatures were maintained at 37°C with a heating pad. The virus solution was stereotaxically injected with a pulled-glass pipette (Drummond #5-000-2005) using an oil-hydraulic pump (Narishige #MO-10).

### Stereotaxic coordinates

Anterior-posterior (AP) and medial-lateral (ML) coordinates are from the bregma, and dorsal-ventral (DV) coordinates are from the brain surface. Stereotaxic coordinates were as follows: nucleus ambiguous (NA): AP: -6.4 mm, ML: -1.2 mm, DV: -4.8 mm; RA: AP: -5.8 mm, ML: 1.2 mm, DV: -5.4 mm (20° AP angle); and PAG: AP: -3.3 mm, ML: 0.6 mm, DV: -2.4 mm (30° AP angle).

### Head-post and optic fiber implantation

In cases of the head-fixed or optogenetic experiments, mice were implanted with a head post (custom-made steel). For optogenetic manipulations, optic cannulas (200-μm core, 0.4 numerical aperture; RWD Life Science) were implanted. The implantations were performed right after the virus injections. Dental cement (C&B Metabond) was applied to the skulls to secure the implantations.

### Three-step monosynaptic tracing for premotor neurons of laryngeal muscles in adult mice

Laryngeal premotor neurons in adult mice were traced by the three-step monosynaptic rabies virus tracing as previously described (27). Briefly, mice pups were anesthetized by isoflurane (3% for induction and 1.5% for maintenance). Midline incision in the neck skin and sternohyoid muscle was performed, and the incised sternohyoid muscle was bilaterally retracted with thin thread to expose the larynx. AAV2retro-hSyn-Cre was injected into laryngeal muscles (500 nl) using a quartz mi-

cropipette (Sutter Instrument) through a microsyringe pump system (UMP3 and Micro4, WPI). Three weeks or more after the AAV injection, a mixture of AAV2/8-CAG-Flex-oG and AAV2/8-CAG-Flex-TVA-mCherry (120 nl total with a 1:1 ratio in volume) was stereotaxically injected in the ipsilateral NA. Two weeks later, EnvA (M21)-RV-ΔG-GFP (200 nl) was injected in the same injection target. After 5 days, the mice were perfused for histology.

### Registering neurons in the Allen CCF

Registrations of laryngeal premotor and RA<sup>VOC</sup> neurons were performed as described previously (27). Briefly, all neurons in serial-sectioned (80-μm) brain slices were manually registered to generate three-dimensional (3D) coordinates in the Allen CCF with custom-written MATLAB. A Python package, Brainrender2 (45), was used to visualize neurons in 3D.

### Analysis of spatial distribution and correlation

As previously described (27), a kernel density estimation in 3D was applied to the 3D coordinates of registered cells. For 2D density plots, the 3D density estimations were projected to 2D dimension (AP, ML, or DV). The 3D density estimations were vectorized, and then cosine similarities were calculated between each premotor map to plot a cross-correlogram. The coordinates of jaw and tongue premotor neurons were obtained from previous work.

### Histology

Mice were anesthetized with an overdose of isoflurane and perfused with ice-cold 1× phosphate-buffered saline (PBS), followed by 4% paraformaldehyde. The brains were frozen in optimal cutting temperature compound (Sakura Finetek). Eighty-micrometer serial coronal sections were made. Neurotrace blue (1:500, Thermo Fisher Scientific #N21479) was used to visualize neuronal structures.

### Immunohistochemistry for ChAT and Fos

Free-floating immunohistochemistry (IHC) was performed as previously described (46). Coronal brain slices were permeabilized for 3 hours in 1% Triton X-100 in PBS (PBST), followed by the blocking solution (10% Blocking One, Nacalai Tesque, in 0.3% PBST). Floating sections were incubated at 4° for 24 hours with the primary antibody in the blocking solution, and then washed with 1× PBS three times for 10 min each. Secondary antibodies in the blocking solution were applied to the sections for 24 hours at 4°. Tissue sections were rinsed with 1× PBS three times for 10 min each. The washed sections were mounted on slides with Mowiol. For ChAT staining, the primary antibodies were goat (1:500, Sigma #AB144P) and the secondary antibodies were anti-goat (1:500, Alexa Fluor 555, Invitrogen #A21432). For Fos staining, primary antibodies were rabbit (1:4000,

Cell Signaling Technology #2250S) and secondary antibodies were anti-rabbit (1:500, Alexa Fluor Plus 647, Invitrogen #A32795).

### Fluorescent HCR (v.3.0, Molecular Instruments) RNA-FISH

Hybridization chain reaction (HCR) was performed as previously described (46). In brief, floating brain sections were perfused in 70% ethanol/PBS overnight at 4°C. The sections were washed with DEPC-PBS for 3 min each. The sections were then treated with 5% SDS/DEPC-PBS for 45 min at room temperature. After rinsing in 2× SSC, the sections were incubated in 2× SSC for 15 min. The sections were then incubated in probe hybridization buffer for 30 min at 37°C for 30 min, followed by incubation with probes (*Fos*, *Vglut2*, *Vgat*, Molecular Instruments) overnight at 37°C. After washing in HCR probe wash buffer (four times for 15 min at 37°C), the sections were rinsed in 2× SSC (twice for 5 min) and incubated in HCR amplification buffer for 30 min at room temperature. The sections were then incubated for 48 hours at 25°C with appropriate hairpins conjugated with Alexa Fluor (denatured and snap-cooled according to manufacturer's instructions) to visualize hybridization signals. The washed sections with 2× SSC (twice) were mounted on slides with Mowiol.

### Male mice courtship behaviors

Male mice were placed in a glass cylindrical chamber and acclimated for 10 min before being introduced to female partners. Female mice were placed in the chamber for up to 1 hour. The behaviors of the mice were recorded with a camera at 20 frames/s. Ninety minutes or 2 hours after introduction of females and vocalization onsets, the male mice were perfused for *Fos* HCR or Fos immunostaining, respectively.

### CANE-based targeting of RA<sup>VOC</sup> neurons

Before CANE-mediated capturing of RA<sup>VOC</sup>, each virgin male Fos<sup>TVA</sup> mouse was first exposed to a female mouse overnight and then isolated in a single chamber for 1 week to facilitate male vocalization in the subsequent courtship contexts. Male mice were introduced with receptive females in a cylindrical chamber to elicit USVs for up to 1 hour. Two hours after the vocalization onsets, CANE (lenti)-hSyn-Cre and Cre dependent AAV2/8-gene X (600 nl total with 4:1 ratio in volume; gene X: hSyn-Flex-TeLC-P2A-EYFP-WPRE, hSyn-DIO-EGFP, nEF-Con/Foff 2.0-ChRmine-oScarlet) were stereotaxically injected to the RA. For specifically targeting excitatory RA<sup>VOC</sup> neurons, Fos<sup>TVA</sup>/Vglut2-ires-cre mice were used, and CANE (lenti)-hSyn-DIO-tTA, and AAV2/8-TRE3G-geneX (600 nl total with 4:1 ratio in volume; gene X: GFP-GFE3, GFP) were injected into the RA.

### PreRAM<sup>VOC</sup> tracing

PreRAM<sup>VOC</sup> tracing is the same as the other experiment using CANE to express helper viruses AAV2/8-CAG-Flex-oG and AAV2/8-CAG-Flex-TVA-mCherry in RAM<sup>VOC</sup>, followed by stereotaxic injection of EnvA (M21)-RV-ΔG-GFP (200 nl) to RAM two weeks later.

### Recording and analysis of USVs

USVs were recorded with a recording system for ultrasonic-range audio signals (Avisoft-Bioacoustics #CM16/CMPA48AAF-5V). The audio signals were digitized at 250 kHz with an analog-digital converter (National Instruments #PCIe-6321). Spectrogram of audio signals were calculated by the short time Fourier transform algorithm (512 Hanning window with 25% overlap). USVs were detected by manual selection from the spectrograms within 30 to 125 kHz. Classification of RAM<sup>VOC</sup>-USVs were manually performed based on the criteria previously described (35). Four acoustic features were calculated for each USV syllable: (i) loudness (average band power between minimum and maximum frequency of each USV syllable as dB relative to background noise in the recording); (ii) spectral purity (relative power of dominant frequency); (iii) mean frequency (averaged dominant frequency at each time point); and (iv) pitch variance (the variance of dominant frequencies). Putative inspiratory vocalizations were manually selected, based on two criteria: being time-locked to inspiration periods and having broad spectral representation.

### Respiratory activity recording and analysis

Respiratory Activity was measured as previously described (32). Briefly, awake mice were head-fixed and an airflow sensor (Honeywell #AMW330V) was closely positioned to the nose of the mice. Voltage signals from the sensor were recorded at 250 kHz (National Instruments #PCIe-6321) and down-sampled to 1 kHz for analysis. All breathing signals were normalized by their resting states. The breathing signals were subtracted by the reference value (at no-flow) and divided by the SD of the resting breathing. For labeling flat expirations, custom Julia codes were used to automatically detect flatten respiratory periods. Each negative and positive period of the breathing signals was interpolated and labeled as inspiration ( $-\pi$  to 0) and expiration (0 to  $\pi$ ) phases, respectively. Inspiration peaks were defined as the minimum values during each inspiration period. The inspiration peaks were interpolated to visualize the amplitude changes over time in average.

### Correlation between duration of USVs and expirations

A linear regression model was used to fit a model of duration of USVs and flat expirations.  $R^2$  was calculated to assess the model.

### Calculation of laser stimulation phases

Laser stimulation phases with respect to respiration ( $\Phi_{\text{laser}}$ ) were similarly calculated as previously described (18). Briefly, each negative and positive period of the breathing signals was interpolated and labeled as inspiration ( $-\pi$  to 0) and expiration (0 to  $\pi$ ) phases, respectively. Laser stimulation time relative to the onset of the inspiration was projected on the prior (control) respiratory period to define  $\Phi_{\text{laser}}$  as from  $-\pi$  to  $\pi$ . Each latency and duration of RAM<sup>VOC</sup>-USVs and expiration data with respect to the laser stimulation phases was polynomial fitted using the CurveFit.jl package to visualize the curves of the data.

### Respiratory phase maps of USVs

The onset and offset time of USV syllables were projected onto the respiratory phase map. Vocalizations are classified as inspiratory or expiratory vocalization based on the phase values (negative as inspiratory and positive as expiratory).

### Pain-induced audible squeak experiments

Either tail pinch or electrical foot shock was applied to the mice. For tail-pinch experiments, awake mice were head fixed and allowed to run on a running wheel. Mice tails were gently grabbed with a gloved hand and further pinched to elicit squeaks. Respiratory activities of the mice were measured with the airflow sensor. For electrical foot shock experiments, mice were placed in a foot-shock chamber, and brief electrical foot shock were delivered to the mice ( $<2$  s, 0.5 mA). The behaviors of the mice in the chamber were recorded with a camera (with audible mic) at 20 frames/s. The squeaks from both stimuli were audible and also represented in the USV spectrum range.

### Abdominal EMG recordings

Mice were initially anesthetized by isoflurane (3%) and then further maintained by intraperitoneal injection of the ketamine and xylazine mixture (1 and 0.1 mg/kg, respectively). The skin above abdominal muscles were shaved and opened to expose abdominal muscles. Teflon coated silver wires (bare diameter: 76.2  $\mu\text{m}$ ; AM Systems #785500) were used to record EMG. The insulation was removed from the tips of silver wires (2 mm) for recording. Recording wire was inserted into the abdominal muscle while reference wire was inserted between the skin and fascia above the muscle. An AC amplifier (World Precision Instruments #DAM80) was used to record EMG, and the voltages were filtered (high-pass: 100 Hz; low-pass: 10 kHz) and collected with the same DAQ board (National Instruments #PCIe-6321). The sampling rate for EMG was 250 kHz for simultaneous recording of USVs. The voltage recordings were down-sampled to 20 kHz for analysis. A root-mean-square filter was applied

to visualize the EMG responses. Averaged EMG responses during PAG stimulation (2 s) were normalized by averaged resting EMG responses (1 s) to calculated PAG-evoked EMG.

### Vocal cord imaging and analysis

Mice were initially anesthetized by isoflurane (3%) and then further maintained by intraperitoneal injection of the ketamine and xylazine mixture (1 and 0.1 mg/kg, respectively). The heads of mice were fixed with clamps, and the mice were put on a flat platform. A round post was placed under the neck to keep the axis of the oral cavity and trachea straight. The tongue was gently pulled out and moved down with a flat metal depressor (custom made) to help visualize the vocal cords. An optic fiber was attached to the tip of the depressor to illuminate the inside of the oral cavities with a red LED (635 nm, Doric). A camera (Basler #acA640-750um) with a lens (Basler Lens #C23-3520-2M-S f50mm) was used to image the vocal cords. Vocal cords were imaged at 100 frames/s. The glottal areas of the vocal cords were calculated by tracking the videos using DeepLabCut (47).

### Optogenetic stimulation of RAM<sup>VOC</sup> and PAG<sup>RAm/Vglut2</sup>

Awake mice were head fixed on a running wheel, and respiratory activities and sound productions were measured together. Bilateral (RAM<sup>VOC</sup>-ChRmine) optogenetic stimulation was applied through optic fibers (0.39 numerical aperture, 200- $\mu\text{m}$  core). A 560-nm laser ( $<10$  mW at the tips) was used, and the stimulation parameters were modulated by TTL pulses with PulsePals. In experiments with RAM<sup>VOC</sup>-GFE3 or control mice, optogenetic stimulation of the PAG was used to elicit USVs in a head-fixed setup. AAV2retro-hSyn-FlpO was injected into the RAM, and Cre/Flp-codependent AAV2/8-nEF-Con/Fon-ChRmine-mScarlet was injected into the PAG.

### Statistics

All data are represented as mean  $\pm$  SEM. Statistical analyses were performed in Julia using the HypothesisTests.jl package. Nonparametric Mann-Whitney  $U$  test was used to compare respiratory modulation in RAM<sup>VOC</sup>-TeLC and RAM<sup>VOC</sup>-GFP mice, mean frequency of RAM<sup>VOC</sup>-USVs over female-directed USVs, and changes in inspiration peaks in RAM<sup>VOC</sup>-GFE3 and RAM<sup>VOC</sup>-GFP mice.

### REFERENCES AND NOTES

- G. Holstege, H. H. Subramanian, Two different motor systems are needed to generate human speech. *J. Comp. Neurol.* **524**, 1558–1577 (2016). doi: 10.1002/cne.23898; pmid: 26355872
- A. Nieder, R. Mooney, The neurobiology of innate, volitional and learned vocalizations in mammals and birds. *Philos. Trans. R. Soc. Lond. B Biol. Sci.* **375**, 20190054 (2020). doi: 10.1098/rstb.2019.0054; pmid: 31735150
- Z. Zhang, Mechanics of human voice production and control. *J. Acoust. Soc. Am.* **140**, 2614–2635 (2016). doi: 10.1121/1.4964509; pmid: 27794319

4. C. A. Del Negro, G. D. Funk, J. L. Feldman, Breathing matters. *Nat. Rev. Neurosci.* **19**, 351–367 (2018). doi: [10.1038/s41583-018-0003-6](https://doi.org/10.1038/s41583-018-0003-6); pmid: 29740175
5. K. L. Christopher et al., Vocal-cord dysfunction presenting as asthma. *N. Engl. J. Med.* **308**, 1566–1570 (1983). doi: [10.1056/NEJM198306303082605](https://doi.org/10.1056/NEJM198306303082605); pmid: 6406891
6. J. M. Hintze, C. L. Ludlow, S. F. Bansberg, C. H. Adler, D. G. Lott, Spasmodic Dysphonia: A Review. Part 2: Characterization of Pathophysiology. *Otolaryngol. Head Neck Surg.* **157**, 558–564 (2017). doi: [10.1177/0194599817728465](https://doi.org/10.1177/0194599817728465); pmid: 28850796
7. U. Jürgens, S. R. Hage, On the role of the reticular formation in vocal pattern generation. *Behav. Brain Res.* **182**, 308–314 (2007). doi: [10.1016/j.bbr.2006.11.027](https://doi.org/10.1016/j.bbr.2006.11.027); pmid: 17173983
8. K. Shiba, T. Urnezaki, Y. Zheng, A. D. Miller, The nucleus retroambiguus controls laryngeal muscle activity during vocalization in the cat. *Exp. Brain Res.* **115**, 513–519 (1997). doi: [10.1007/PL00005721](https://doi.org/10.1007/PL00005721); pmid: 9262206
9. S. P. Zhang, R. Bandler, P. J. Davis, Brain stem integration of vocalization: Role of the nucleus retroambiguus. *J. Neurophysiol.* **74**, 2500–2512 (1995). doi: [10.1152/jn.1995.74.6.2500](https://doi.org/10.1152/jn.1995.74.6.2500); pmid: 8747209
10. K. Hartmann, M. Brecht, A Functionally and Anatomically Bipartite Vocal Pattern Generator in the Rat Brainstem. *iScience* **23**, 101804 (2020). doi: [10.1016/j.isci.2020.101804](https://doi.org/10.1016/j.isci.2020.101804); pmid: 33299974
11. S. P. Zhang, P. J. Davis, P. Carrive, R. Bandler, Vocalization and marked pressor effect evoked from the region of the nucleus retroambiguus in the caudal ventrolateral medulla of the cat. *Neurosci. Lett.* **140**, 103–107 (1992). doi: [10.1016/0304-3940\(92\)90692-Z](https://doi.org/10.1016/0304-3940(92)90692-Z); pmid: 1383887
12. L. Lütke, U. Häusler, U. Jürgens, Neuronal activity in the medulla oblongata during vocalization. A single-unit recording study in the squirrel monkey. *Behav. Brain Res.* **116**, 197–210 (2000). doi: [10.1016/S0166-4328\(00\)00272-2](https://doi.org/10.1016/S0166-4328(00)00272-2); pmid: 11080551
13. M. Concha-Miranda, W. Tang, K. Hartmann, M. Brecht, Large-Scale Mapping of Vocalization-Related Activity in the Functionally Diverse Nuclei in Rat Posterior Brainstem. *J. Neurosci.* **42**, 8252–8261 (2022). doi: [10.1523/JNEUROSCI.0813-22.2022](https://doi.org/10.1523/JNEUROSCI.0813-22.2022); pmid: 36113990
14. G. Holstege, Anatomical study of the final common pathway for vocalization in the cat. *J. Comp. Neurol.* **284**, 242–252 (1989). doi: [10.1002/cne.902840208](https://doi.org/10.1002/cne.902840208); pmid: 2754035
15. H. H. Subramanian, G. Holstege, The nucleus retroambiguus control of respiration. *J. Neurosci.* **29**, 3824–3832 (2009). doi: [10.1523/JNEUROSCI.0607-09.2009](https://doi.org/10.1523/JNEUROSCI.0607-09.2009); pmid: 19321779
16. Y. Cui et al., Defining preBötzing Complex Rhythm- and Pattern-Generating Neural Microcircuits In Vivo. *Neuron* **91**, 602–614 (2016). doi: [10.1016/j.neuron.2016.07.003](https://doi.org/10.1016/j.neuron.2016.07.003); pmid: 27497222
17. A. Huff, M. Karlen-Amarante, T. Pitts, J. M. Ramirez, Optogenetic stimulation of pre-Bötzing complex reveals novel circuit interactions in swallowing-breathing coordination. *Proc. Natl. Acad. Sci. U.S.A.* **119**, e2121095119 (2022). doi: [10.1073/pnas.2121095119](https://doi.org/10.1073/pnas.2121095119); pmid: 35858334
18. D. Sherman, J. W. Worrell, Y. Cui, J. L. Feldman, Optogenetic perturbation of preBötzing complex inhibitory neurons modulates respiratory pattern. *Nat. Neurosci.* **18**, 408–414 (2015). doi: [10.1038/nn.3938](https://doi.org/10.1038/nn.3938); pmid: 25643296
19. J. C. Smith, H. H. Ellenberger, K. Ballanyi, D. W. Richter, J. L. Feldman, Pre-Bötzing complex: A brainstem region that may generate respiratory rhythm in mammals. *Science* **254**, 726–729 (1991). doi: [10.1126/science.1683005](https://doi.org/10.1126/science.1683005); pmid: 1683005
20. S. Tupal et al., Testing the role of preBötzing Complex somatostatin neurons in respiratory and vocal behaviors. *Eur. J. Neurosci.* **40**, 3067–3077 (2014). doi: [10.1111/ejn.12669](https://doi.org/10.1111/ejn.12669); pmid: 25040660
21. G. Arriaga, E. D. Jarvis, Mouse vocal communication system: Are ultrasounds learned or innate? *Brain Lang.* **124**, 96–116 (2013). doi: [10.1016/j.bandl.2012.10.002](https://doi.org/10.1016/j.bandl.2012.10.002); pmid: 23295209
22. T. E. Holy, Z. Guo, Ultrasonic songs of male mice. *PLOS Biol.* **3**, e386 (2005). doi: [10.1371/journal.pbio.0030386](https://doi.org/10.1371/journal.pbio.0030386); pmid: 16248680
23. M. Fernández-Vargas, T. Riede, B. Pasch, Mechanisms and constraints underlying acoustic variation in rodents. *Anim. Behav.* **184**, 135–147 (2022). doi: [10.1016/j.anbehav.2021.07.011](https://doi.org/10.1016/j.anbehav.2021.07.011)
24. J. Håkansson et al., Aerodynamics and motor control of ultrasonic vocalizations for social communication in mice and rats. *BMC Biol.* **20**, 3 (2022). doi: [10.1186/s12915-021-01185-z](https://doi.org/10.1186/s12915-021-01185-z); pmid: 34996429
25. E. Mahrt, A. Agarwal, D. Perkel, C. Portfors, C. P. H. Elemans, Mice produce ultrasonic vocalizations by intra-laryngeal planar impinging jets. *Curr. Biol.* **26**, R880 (2016). doi: [10.1016/j.cub.2016.08.032](https://doi.org/10.1016/j.cub.2016.08.032); pmid: 27728788
26. T. Riede, H. L. Borgard, B. Pasch, Laryngeal airway reconstruction indicates that rodent ultrasonic vocalizations are produced by an edge-tone mechanism. *R. Soc. Open Sci.* **4**, 170976 (2017). doi: [10.1098/rsos.170976](https://doi.org/10.1098/rsos.170976); pmid: 29291091
27. J. Takatoh et al., Constructing an adult orofacial premotor atlas in Allen mouse CCF. *eLife* **10**, e67291 (2021). doi: [10.7554/eLife.67291](https://doi.org/10.7554/eLife.67291); pmid: 33904410
28. J. Håkansson et al., The Allen Mouse Brain Common Coordinate Framework: A 3D Reference Atlas. *Cell* **181**, 936–953.e20 (2020). doi: [10.1016/j.cell.2020.04.007](https://doi.org/10.1016/j.cell.2020.04.007); pmid: 32386544
29. K. Sakurai et al., Capturing and manipulating activated neuronal ensembles with CANE delineates a hypothalamic social-fear circuit. *Neuron* **92**, 739–753 (2016). doi: [10.1016/j.neuron.2016.10.015](https://doi.org/10.1016/j.neuron.2016.10.015); pmid: 27974160
30. G. Schiavo et al., Tetanus and botulinum-B neurotoxins block neurotransmitter release by proteolytic cleavage of synaptobrevin. *Nature* **359**, 832–835 (1992). doi: [10.1038/359832a0](https://doi.org/10.1038/359832a0); pmid: 1331807
31. J. Ruat et al., Why do mice squeak? Toward a better understanding of defensive vocalization. *iScience* **25**, 104657 (2022). doi: [10.1016/j.isci.2022.104657](https://doi.org/10.1016/j.isci.2022.104657); pmid: 35845167
32. K. Tschida et al., A Specialized Neural Circuit Gates Social Vocalizations in the Mouse. *Neuron* **103**, 459–472.e4 (2019). doi: [10.1016/j.neuron.2019.05.025](https://doi.org/10.1016/j.neuron.2019.05.025); pmid: 31204083
33. C. Hérent, S. Diem, G. Fortin, J. Bouvier, Absent phasing of respiratory and locomotor rhythms in running mice. *eLife* **9**, e61919 (2020). doi: [10.7554/eLife.61919](https://doi.org/10.7554/eLife.61919); pmid: 33258770
34. K. E. Kishi et al., Structural basis for channel conduction in the pump-like channelrhodopsin ChRmine. *Cell* **185**, 672–689.e23 (2022). doi: [10.1016/j.cell.2022.01.007](https://doi.org/10.1016/j.cell.2022.01.007); pmid: 35114111
35. A. H. O. Fonseca, G. M. Santana, G. M. Bosque Ortiz, S. Bampi, M. O. Dietrich, Analysis of ultrasonic vocalizations from mice using computer vision and machine learning. *eLife* **10**, e59161 (2021). doi: [10.7554/eLife.59161](https://doi.org/10.7554/eLife.59161); pmid: 33787490
36. C. F. Yang, J. L. Feldman, Efferent projections of excitatory and inhibitory preBötzing Complex neurons. *J. Comp. Neurol.* **526**, 1389–1402 (2018). doi: [10.1002/cne.24415](https://doi.org/10.1002/cne.24415); pmid: 29473167
37. G. G. Gross et al., An E3-ligase-based method for ablating inhibitory synapses. *Nat. Methods* **13**, 673–678 (2016). doi: [10.1038/nmeth.3894](https://doi.org/10.1038/nmeth.3894); pmid: 27271196
38. I. A. Volodin, D. Yurlova, O. G. Ilchenko, E. V. Volodina, Ontogeny of audible squeaks in yellow steppe lemming *Eolagus luteus*: Trend towards shorter and low-frequency calls is reminiscent of those in ultrasonic vocalization. *BMC Zool.* **6**, 27 (2021). doi: [10.1186/s40850-021-00092-8](https://doi.org/10.1186/s40850-021-00092-8); pmid: 37170373
39. M. Smotherman, K. Kobayasi, J. Ma, S. Zhang, W. Metzner, A mechanism for vocal-respiratory coupling in the mammalian parabrachial nucleus. *J. Neurosci.* **26**, 4860–4869 (2006). doi: [10.1523/JNEUROSCI.4607-05.2006](https://doi.org/10.1523/JNEUROSCI.4607-05.2006); pmid: 16672660
40. J. W. Arthurs, A. J. Bowen, R. D. Palmiter, N. A. Baertsch, Parabrachial tachykinin1-expressing neurons involved in state-dependent breathing control. *Nat. Commun.* **14**, 963 (2023). doi: [10.1038/s41467-023-36603-z](https://doi.org/10.1038/s41467-023-36603-z); pmid: 36810601
41. S. Liu et al., Divergent brainstem opioidergic pathways that coordinate breathing with pain and emotions. *Neuron* **110**, 857–873.e9 (2022). doi: [10.1016/j.neuron.2021.11.029](https://doi.org/10.1016/j.neuron.2021.11.029); pmid: 34921781
42. X. P. Wei, M. Collie, B. Dempsey, G. Fortin, K. Yackle, A novel reticular node in the brainstem synchronizes neonatal mouse crying with breathing. *Neuron* **110**, 644–657.e6 (2022). doi: [10.1016/j.neuron.2021.12.014](https://doi.org/10.1016/j.neuron.2021.12.014); pmid: 34998469
43. K. Yackle, Transformation of our understanding of breathing control by molecular tools. *Annu. Rev. Physiol.* **85**, 93–113 (2023). doi: [10.1146/annurev-physiol-021522-094142](https://doi.org/10.1146/annurev-physiol-021522-094142); pmid: 36323001
44. K. Nakazawa et al., Role of pulmonary afferent inputs in vocal on-switch in the cat. *Neurosci. Res.* **29**, 49–54 (1997). doi: [10.1016/S0168-0102\(97\)00071-0](https://doi.org/10.1016/S0168-0102(97)00071-0); pmid: 9293492
45. F. Claudi, A. L. Tyson, L. Petrucco, T. W. Margrie, R. Portugues, T. Branco, *Brainrender*: A python-based software for visualizing anatomically registered data. *bioRxiv* 961748 [Preprint] (2020). <https://doi.org/10.1101/2020.02.23.961748>
46. J. Takatoh et al., The whisking oscillator circuit. *Nature* **609**, 560–568 (2022). doi: [10.1038/s41586-022-05144-8](https://doi.org/10.1038/s41586-022-05144-8); pmid: 36045290
47. T. Nath et al., Using DeepLabCut for 3D markerless pose estimation across species and behaviors. *Nat. Protoc.* **14**, 2152–2176 (2019). doi: [10.1038/s41596-019-0176-0](https://doi.org/10.1038/s41596-019-0176-0); pmid: 31227823
48. Data for: J. Park, S. Choi, J. Takatoh, S. Zhao, A. Harrahill, B.-X. Han, F. Wang, Brainstem control of vocalization and its coordination with respiration, *Dryad* (2024); <https://doi.org/10.5061/dryad.vmcvndm0m>

## ACKNOWLEDGMENTS

We thank D. Kleinfeld, V. Prevosto, and P. Thompson for critically reading the manuscript; members of the Wang lab for technical help and suggestions during the entire process of this research project; and members of the Richard Mooney lab for stimulating discussions on vocalization circuits and mechanisms. **Funding:** This work was supported by the National Institutes of Health (grant MH117778 to F.W. and grant NS107466, a team grant with a subaward to F.W.). **Author contributions:** F.W. and J.P. conceptualized the project, designed experiments, and wrote the paper with input from all authors. J.P. performed the majority of experiments. J.P. and J.T. analyzed data. S.C. performed histology works. S.Z., A.H., and J.T. produced key viral vectors used in this study. B.H. and S.C. provided animal husbandry. F.W. supervised all the work. **Competing interests:** The authors declare no competing interests. **Data and materials availability:** All data are available in the manuscript or supplementary materials and have been deposited at Dryad (48). **License information:** Copyright © 2024 the authors, some rights reserved; exclusive licensee American Association for the Advancement of Science. No claim to original US government works. <https://www.science.org/about/science-licenses-journal-article-reuse>

## SUPPLEMENTARY MATERIALS

[science.org/doi/10.1126/science.adi8081](https://science.org/doi/10.1126/science.adi8081)

Figs. S1 to S6  
Movies S1 to S3  
MDAR Reproducibility Checklist

Submitted 18 May 2023; resubmitted 21 November 2023

Accepted 18 January 2024

10.1126/science.adi8081